ACS OMEGA

Open Access

http://pubs.acs.org/journal/acsodf

Article

Tuning Pd-to-Ag Ratio to Enhance the Synergistic Activity of Fly Ash-Supported Pd_xAg_y Bimetallic Nanoparticles

Niladri Maity,* Aman Mishra, Samir Barman, Sumanta Kumar Padhi, Binod Bihari Panda, E. A. Jaseer, and Mohamed Javid

Cite This: *ACS Omega* 2024, 9, 1020−1028

Read Online

ACCESS | Metrics & More | Article Recommendations | Supporting Information

ABSTRACT: Fly ash (FA)-supported bimetallic nanoparticles (Pd_xAg_y/FA) with varying Pd:Ag ratios were prepared by coprecipitation of Pd and Ag involving in situ reduction of Pd(II) and Ag(I) salts in aqueous medium. All the supported nanoparticles were thoroughly characterized with the aid of powder X-ray diffraction (PXRD), X-ray photoelectron spectroscopy (XPS), electron microscopy (field emission scanning electron microscopy (FE-SEM) and transmission electron microscopy (TEM)), and elemental analyses, which include inductively coupled plasma-optical emission spectroscopy (ICP-OES) and energy-dispersive X-ray spectroscopy (EDS). A gradual broadening and shifting of PXRD peaks, ascribable to Ag, to higher angles with an increase in the Pd:Ag ratio affirms the alloying of interface between Pd and Ag nanoparticles. The coexistence of Pd and Ag was further confirmed by EDS elemental mapping as well as by the presence of bimetallic lattices on the FA surface, as evident from the high-resolution TEM analysis. The dependency of crystallite size and average size of bimetallic nanoparticles on Ag loading (mol %) was elucidated with the help of a combination of PXRD and TEM studies. Based on XPS analysis, the charge transfer phenomenon between contacting Pd−Ag sites could be evident from the shifting of 3d core electron binding energy for both Pd and Ag compared with monometallic Pd and Ag nanoparticles. Following a pseudo-first-order reaction kinetics, all the nanocatalysts were able to efficiently reduce 4-nitrophenol into 4-aminophenol in aqueous $NaBH_4$. The superior catalytic performance of the bimetallic nanocatalysts (Pd_xAg_y/FA) over their monometallic (Pd_{100}/FA and Ag_{100}/FA) analogues has been demonstrated. Moreover, the tunable synergistic effect of the bimetallic systems has been explored in detail by varying the Pd:Ag mol ratio in a systematic manner which in turn allowed us to achieve an optimum reaction rate (k = 1.050 min^{-1}) for the nitrophenol reduction using a $Pd_{25}Ag_{75}$/FA system. Most importantly, all the bimetallic nanocatalysts explored here exhibited excellent normalized rate constants ($K \approx$ 6000−15,000 min^{-1} $mmol^{-1}$) compared with other supported bimetallic Pd−Ag nanocatalysts reported in the literature.

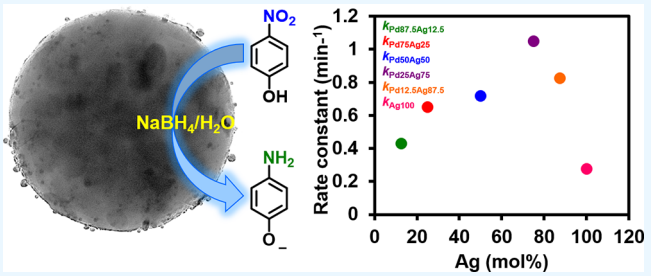

INTRODUCTION

Bimetallic nanoparticles exhibiting versatile and tunable shape-, size-, and composition-dependent properties have gained immense research attention due to their widespread application in catalysis, fuel cells, organic reactions, and sensing devices.[1−6] The superiority of bimetallic systems over their monomeric analogous is often associated with the metal−metal interaction and charge separation between the hetero atoms.[7−10] By taking advantage of these features, a number of important organic transformations including CO and oxygen reduction,[11−13] oxidation reaction,[14] dechlorination reaction,[15] CO_2 hydrogenation,[16] and dry reforming reaction[17] at high efficiency have been achieved.

Catalytic reduction of highly toxic nitroaromatics into commercially demanding amine derivatives by using appropriate heterometallic nanocatalysts has gained significant current research interest.[18−23] In particular, Pd-based systems, such as Pd−Au, Pd−Cu, Pd−Ni, Pd−Pt, and Pd−Ag, have been studied extensively.[18,19,24−26] Considering Ag is less electronegative (1.9) than Pd (2.2), the incorporation of Ag in the lattice of Pd has been exploited to realize potential charge redistribution and superior catalytic performance.[27−29] Since Pd−Ag bimetallic nanostructure can form a solid solution,[30] a gradual incorporation of Ag atom into Pd lattice was anticipated to elevate the catalytic activity and hence the atom economy. Nevertheless, the ratio between Pd and Ag in the bimetallic system was also believed to play a pivotal role in achieving optimum catalytic performance.[31] Moreover, Ag being a less active counterpart, an excess presence of it beyond a critical level was presumed to exhibit detrimental effects. In fact, Sun et al. reported that among the bimetallic nano-

Received: September 20, 2023
Revised: October 23, 2023
Accepted: December 5, 2023
Published: December 20, 2023

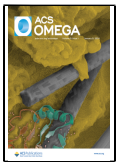

particles with varying Pd:Ag ratios ($Pd_{29}Ag_{71}$, $Pd_{56}Ag_{44}$, $Pd_{64}Ag_{36}$, $Pd_{70}Ag_{30}$, and $Pd_{88}Ag_{12}$), the optimum activity for the generation of hydrogen from ammonia borane (via methanolysis) could be achieved by the $Pd_{70}Ag_{30}$ system.[32]

Dispersion of metal nanoparticles on a suitable support is an important aspect of catalysis as this provides stability to the nanoparticles by restricting their agglomeration and retaining catalytic activity under a wide range of reaction conditions.[33−36] In our previous study,[29] we have shown for the first time that Pd−Ag bimetallic nanoparticles supported on fly ash (FA), a good absorption solid material primarily composed of silica and alumina,[37−40] could exhibit an excellent synergistic activity toward reducing 4-nitrophenol in aqueous $NaBH_4$ medium under ambient conditions. Herein, we report an easy synthesis method, an alternative of relatively costly, more time-consuming, and involving complex reaction steps such as hydrothermal method,[41] electrochemical deposition,[42] seed-mediated growth,[43] and galvanic replacement,[41] to prepare novel FA-supported bimetallic nanoparticles (Pd_xAg_y/FA). The impact of Pd:Ag ratio toward tuning the synergistic effect of the bimetallic system to efficiently reduce nitrophenol into aminophenol in an aqueous $NaBH_4$ medium (Scheme 1) has been investigated. Moreover, a structure−activity correlation has been explored with the help of microscopic and spectroscopic analysis techniques.

Scheme 1. Schematic Representation of the Bimetallic Nanoparticle Synthesis and the Targeted Catalytic Transformation of Nitrophenol to Aminophenol Using FA-Supported Monometallic (Pd_{100}/FA and Ag_{100}/FA) and Bimetallic (Pd_xAg_y/FA) Nanocatalysts in Aqueous $NaBH_4$ Solution

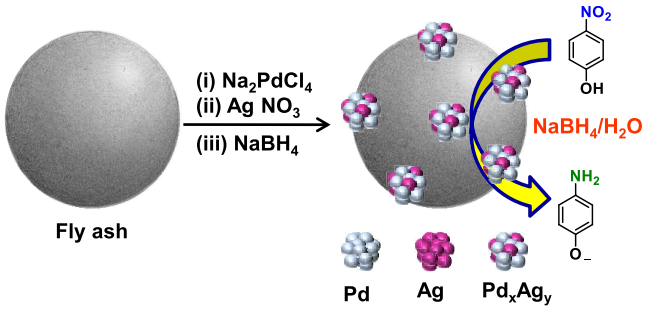

EXPERIMENTAL SECTION

General Procedures. All of the chemicals purchased from the commercial sources were used as received. Deionized water was used for the preparation of all of the aqueous solutions. FA was collected from National Aluminum Company Limited (NALCO), Bhubaneswar, India.

Instrumentation. Powder X-ray diffraction (PXRD) of the nanomaterials was conducted using a Rigaku diffractometer (40 kV and 40 mA) equipped with Cu Kα radiation (λ = 1.54 Å) at a scanning rate 4°/min and within a 2θ range of 10−110°. The average crystallite sizes (D) of Pd, Ag, and Pd_xAg_y in Pd_{100}/FA, $Pd_{87.5}Ag_{12.5}$/FA, $Pd_{75}Ag_{25}$/FA, $Pd_{50}Ag_{50}$/FA, $Pd_{25}Ag_{75}$/FA, $Pd_{12.5}Ag_{87.5}$/FA, and Ag_{100}/FA were evaluated using the Debye−Scherrer equation $D = K\lambda/(\beta \cos \theta)$, where K is the Scherrer constant (0.89), λ is the X-ray wavelength (0.154 nm), β is the full-width at half-maxima of the diffraction peak, and θ is the diffraction angle.[44−46] Advanced PHI-5000 Versa-probe setup was used to perform an X-ray photoelectron spectroscopic (XPS) study. The binding energies were referenced to the adventitious C 1s peak at 284.8 eV.[47] The field emission scanning electron microscopy (FE-SEM) and energy-dispersive X-ray spectroscopy (EDS) studies were performed using the Zeiss SUPRA 55-VP instrument. The JEOL-JEM 2100 electron microscope was used to collect high-resolution transmission electron microscopy (HR-TEM) images, where the samples were prepared by sonicating suspended nanomaterials in ethanol, followed by depositing the suspension on carbon-coated copper grids. Inductively coupled plasma-optical emission spectroscopy (ICP-OES) related analyses were conducted on Thermo Fisher Scientific (iCAP 7400 Duo) equipment. The UV−visible spectra of liquid samples were collected using a Neumann & Müller NM-1900S spectrophotometer.

Preparation of FA-Supported Pd Nanoparticles (Pd_{100}/FA). Over a slurry of FA (1 g) in water (5 mL), an aqueous solution (5 mL) of Na_2PdCl_4 (28 mg, 0.095 mmol) was added under stirring at ambient temperature. After the stirring was continued for 30 min, a freshly prepared 5 mL solution of $NaBH_4$ (0.095M) was added dropwise over a time period of 2 min. After 1 h, FA-supported Pd nanoparticles (Pd_{100}/FA) were filtered and sequentially washed with water and acetone. Finally, the solid material was dried under a dynamic vacuum for 2 h at 50 °C.

Preparation of FA-Supported Ag Nanoparticles (Ag_{100}/FA). An aqueous solution (5 mL) of $AgNO_3$ (16 mg, 0.094 mmol) was added to a slurry of FA (1.0 g) in water (5 mL) under stirring. After 30 min, a freshly prepared 5 mL of aqueous $NaBH_4$ solution (0.094 M) was added at room temperature. After continuing the stirring for another 1 h, the FA-supported Ag nanoparticles (Ag_{100}/FA) were filtered and washed subsequently with water and acetone. Finally, the solid material was dried under a dynamic vacuum for 2 h at 50 °C.

Preparation of FA-Supported Pd_xAg_y Bimetallic Nanoparticles (Pd_xAg_y/FA). *Preparation of $Pd_{87.5}Ag_{12.5}$/FA.* Over a slurry of FA (1.0 g) in water (5 mL), aqueous solutions (5 mL each) of Na_2PdCl_4 (24.5 mg, 0.082 mmol) and $AgNO_3$ (2 mg, 0.0117 mmol) were added consecutively. After 30 min, a freshly prepared $NaBH_4$ solution (5 mL) in water (0.094 M) was added to the mixture over 5 min at ambient temperature. After stirring was continued for 1 h, the material was filtered and washed with water and acetone. Finally, the FA-supported $Pd_{87.5}Ag_{12.5}$ nanoparticles ($Pd_{87.5}Ag_{12.5}$/FA) was dried at 50 °C under a dynamic vacuum for 2 h.

Preparation of $Pd_{75}Ag_{25}$/FA, $Pd_{50}Ag_{50}$/FA, $Pd_{25}Ag_{75}$/FA, and $Pd_{12.5}Ag_{87.5}$/FA. For the preparation of (i) $Pd_{75}Ag_{25}$/FA, Na_2PdCl_4 (21 mg, 0.0705 mmol) and $AgNO_3$ (4 mg, 0.0235 mmol); (ii) $Pd_{50}Ag_{50}$/FA, Na_2PdCl_4 (14 mg, 0.047 mmol) and $AgNO_3$ (8 mg, 0.047 mmol); (iii) $Pd_{25}Ag_{75}$/FA, Na_2PdCl_4 (7 mg, 0.0235 mmol) and $AgNO_3$ (12 mg, 0.705 mol); and (iv) $Pd_{12.5}Ag_{87.5}$/FA, Na_2PdCl_4 (3.5 mg, 0.0117 mmol) and $AgNO_3$ (14 mg, 0.08225 mmol) were considered while keeping all the other reaction parameters used for the synthesis of $Pd_{87.5}Ag_{12.5}$/FA unchanged.

The experimental Pd and Ag loadings of all the monometallic (Pd_{100}/FA and Ag_{100}/FA) and bimetallic (Pd_xAg_y/FA) nanoparticles were estimated using ICP-OES analysis (Table S1).

Catalytic Reduction of 4-Nitrophenol Using FA-Supported Nanoparticles. Catalytic reduction of 4-nitro-

https://doi.org/10.1021/acsomega.3c07246
ACS Omega 2024, 9, 1020−1028

phenol (4-NP) into 4-aminophenol (4-AP) was monitored by UV−visible spectroscopy within the range of 210−550 nm. First, aqueous solutions of 4-NP (0.1 mM, 1.5 mL) and $NaBH_4$ (10 mM, 1.5 mL) were added sequentially to a quartz cuvette. The catalytic reaction was started after the addition of 0.5 mL of dispersed Pd_{100}/FA (2 mg/mL H_2O) into the 4-NP and $NaBH_4$ mixture. Reduction of 4-NP was measured from a change in the absorption intensity of the band appearing at 400 nm. UV−visible spectra were collected at different time intervals to study the reaction kinetics.

Similarly, an equimolar metal was employed in every catalytic run under identical conditions to conduct the reduction of 4-NP using Ag_{100}/FA and Pd_xAg_y/FA nanomaterials.

Since a large excess (ca. 100 times) of $NaBH_4$ was typically used as compared to the substrate 4-NP, the reaction rate can be considered independent of $NaBH_4$ concentration. Therefore, the rate of the reaction can be expressed as $-(dC/dt) = kC$ or $\ln(C/C_0) = -kt$, where C and C_0 are the 4-NP concentrations at times t and 0, respectively. The rate constant is represented by k. The ratio of C/C_0 can directly be obtained from the ratio of A/A_0 (absorbance intensity of 4-NP at time 0 and time t, respectively). The rate constant (k) of the reaction can be received from the slope of the straight line in a $\ln(C/C_0)$ vs time (t) plot.

The recyclability of $Pd_{25}Ag_{75}$/FA nanocatalyst for the reduction of 4-NP was tested following a slightly modified literature protocol.[22,23] In the beginning, 50 μL (3 M) of 4-NP was added to a quartz cuvette, followed by sequential addition of 1.5 mL of water and 1.5 mL (0.1 M) of freshly prepared aqueous $NaBH_4$ solution. Catalytic reaction was started by adding 0.5 mL of dispersed $Pd_{25}Ag_{75}$/FA (2 mg/mL) to the reaction mixture. After completion of the first cycle, fresh 50 μL of 4-NP solution was added to start the second cycle, and the procedure was repeated for additional three cycles.

RESULTS AND DISCUSSION

The FA-supported nanoparticles Pd_{100}/FA, Ag_{100}/FA, $Pd_{87.5}Ag_{12.5}$/FA, $Pd_{75}Ag_{25}$/FA, $Pd_{50}Ag_{50}$/FA, $Pd_{25}Ag_{75}$/FA, and $Pd_{12.5}Ag_{87.5}$/FA were prepared by in situ reduction of Pd(II) and Ag(I) precursors in aqueous medium. The isolated and dried samples were characterized using various spectroscopic, microscopic, and analytical techniques.

In order to understand the crystalline nature of the materials, a freshly prepared powder sample of FA, the supported monometallic Pd_{100}/FA and Ag_{100}/FA and bimetallic $Pd_{87.5}Ag_{12.5}$/FA, $Pd_{75}Ag_{25}$/FA, $Pd_{50}Ag_{50}$/FA, $Pd_{25}Ag_{75}$/FA, and $Pd_{12.5}Ag_{87.5}$/FA nanoparticles were analyzed by PXRD (Figure 1A), which reveals that the pristine sample of FA mainly consists of crystalline mullite (JPCDS card number: 15-0776) and quartz (JPCDS card number: 46-1045) phases along with a part of amorphous phase appears as a broad hump in the 2θ range of 20−30° (Figure 1a).[48] No clearly identifiable Pd diffraction peaks (expected at 39.20 and 45.6° for the Pd(111) and Pd(200) lattice planes, respectively (JCPDS card number: 05-0681)),[49] could be observed for Pd containing nanomaterials due to peaks overlapping with mullite (M) phase of FA support. The PXRD spectrum of Ag_{100}/FA (Figure 1B-h), however, exhibited two distinctly isolable peaks at 2θ values of 38.20 and 44.35° corresponding to Ag(111) and Ag(200) lattice planes, respectively (JCPDS card number: 04-0783).[50] Thus, affirming the presence of crystalline Ag nanoparticles in the Ag_{100}/FA sample.

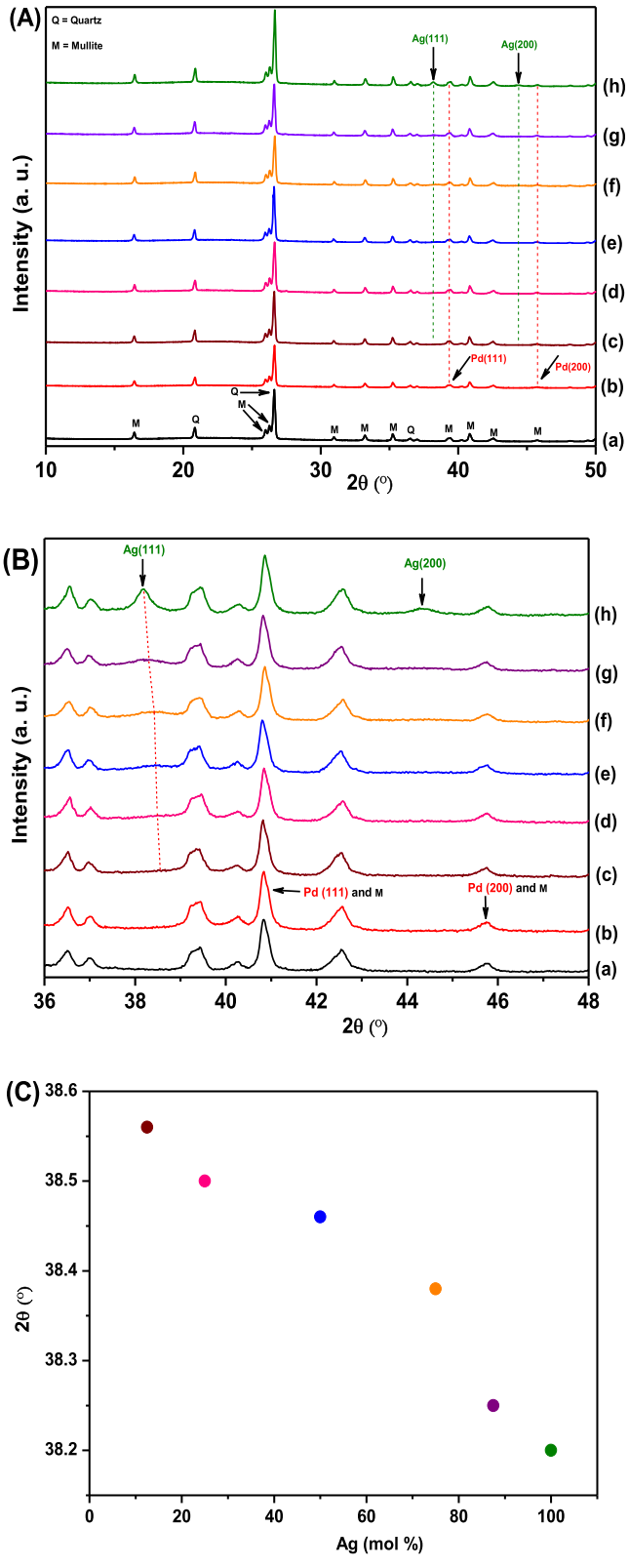

Figure 1. (A) PXRD pattern of (a) FA, (b) Pd_{100}/FA, (c) $Pd_{87.5}Ag_{12.5}$/FA, (d) $Pd_{75}Ag_{25}$/FA, (e) $Pd_{50}Ag_{50}$/FA, (f) $Pd_{25}Ag_{75}$/FA, (g) $Pd_{12.5}Ag_{87.5}$/FA, and (h) Ag_{100}/FA. (B) Expanded view of the PXRD spectra in the 2θ range of 36−48°. (C) Plot of diffraction angle of Ag(111) plane vs Ag mole fraction (%) in $Pd_{87.5}Ag_{12.5}$/FA, $Pd_{75}Ag_{25}$/FA, $Pd_{50}Ag_{50}$/FA, $Pd_{25}Ag_{75}$/FA, $Pd_{12.5}Ag_{87.5}$/FA, and Ag_{100}/FA.

https://doi.org/10.1021/acsomega.3c07246
ACS Omega 2024, 9, 1020−1028

Interestingly, an alteration of the peak position as well as the broadening of the signals corresponding to Ag(111) and Ag(200) lattice planes (Figure 1B-c–h) was observed for all the FA-supported Ag containing bimetallic nanoparticles $Pd_{87.5}Ag_{12.5}$/FA, $Pd_{75}Ag_{25}$/FA, $Pd_{50}Ag_{50}$/FA, $Pd_{25}Ag_{75}$/FA, and $Pd_{12.5}Ag_{87.5}$/FA. Notably, the peak related to Ag(200) lattice plane almost disappeared due to excessive broadening, while the peak corresponding to the Ag(111) plane gradually broadened and shifted to a higher angle with increasing Ag mol % (Figure 1C and Table 1) loading. Such observation led us to assume a potential alloy formation between Pd and Ag interphase.[32,51] Further, the crystallite size of the FA-supported nanoparticles was estimated for $Pd_{87.5}Ag_{12.5}$/FA (8.10 nm), $Pd_{75}Ag_{25}$/FA (8.74 nm), $Pd_{50}Ag_{50}$/FA (9.38 nm), $Pd_{25}Ag_{75}$/FA (9.43 nm), $Pd_{12.5}Ag_{87.5}$/FA (10.20 nm), and Ag_{100}/FA (20.06 nm) using the Debye–Scherrer equation (Table 1). A gradual increase in crystallite size was observed with increasing Ag loading (mol %) for the bimetallic nanomaterials. The dependence of the size of the bimetallic alloy nanoparticles on the metal molar ratio has been reported to be correlated with collision energy, sticking coefficient, rates of nucleation, and growth.[52] Nevertheless, due to peaks overlapping, as discussed earlier (Figure 1B-b), the size of the Pd crystallite could not be determined using the Debye–Scherrer equation.

Table 1. Diffraction Angle for Ag(111) Lattice Plane in Pd_xAg_y/FA and Crystallite Size of the Metal Nanoparticles

Pd_xAg_y/FA	empirical Ag mol %	2θ (°) (Ag(111))	crystallite size (nm)[a]
Pd_{100}/FA	0		ND[b]
$Pd_{87.5}Ag_{12.5}$/FA	12.5	38.56	8.10
$Pd_{75}Ag_{25}$/FA	25	38.52	8.74
$Pd_{50}Ag_{50}$/FA	50	38.46	9.38
$Pd_{25}Ag_{75}$/FA	75	38.38	9.43
$Pd_{12.5}Ag_{87.5}$/FA	87.5	38.25	10.20
Ag_{100}/FA	100	38.20	20.06

[a]Estimated using the Debye–Scherrer equation. [b]Not determined.

The FE-SEM image of FA shows the presence of spherical and agglomerated particles, which are mostly composed of O, Si, Al, Ca, Fe, and Ti atoms, and are complemented by the EDS spectrum (Figure S1 and Table S2). From the element mapping of FA, it could be evident that these elements are evenly distributed throughout the particles (Figure S2). Similarly, the FE-SEM images and element mapping of monometallic Pd_{100}/FA, Ag_{100}/FA also exhibited uniform distribution of Pd and Ag over the surface of FA, while both of these elements coexist in bimetallic Pd_xAg_y/FA systems (Figures S3–S9). The uniform distribution and coexistence of both Pd and Ag further support the formation of an alloy structure in bimetallic Pd_xAg_y/FA systems.

The surface morphology of the supported nanomaterials was further investigated by using TEM analysis. This reveals a clear dispersion of Pd and Ag nanoparticles throughout the support (Figures 2 and S10–S13). The coexistence of Pd and Ag in the bimetallic nanoparticles was also authenticated by EDS elemental mapping (Figures 2c,d and S10–S13c,d). Moreover, the HR-TEM images (Figures 2b and S10–S13b) showing the presence of lattice fringes further confirm the bimetallic crystalline structures of the nanoparticles. While the lattice spacing around 0.224 and 0.195 nm corresponds to the Pd(111) and Pd(200) planes, the spacings of 0.235 and 0.203 nm are likely to be associated with the Ag(111) and Ag(200) planes, respectively.[19,29] Further, the average size of Pd_xAg_y nanoparticles was estimated from TEM images (Figures S16–S22), which was found to increase along with Ag loading (from $Pd_{87.5}Ag_{12.5}$/FA (6.96 nm), $Pd_{75}Ag_{25}$/FA (8.10 nm), Pd_{50}-Ag_{50}/FA (8.16 nm), Pd_{25}–Ag_{75}/FA (8.57 nm) to $Pd_{12.5}Ag_{87.5}$/FA (9.43 nm)). The size of the bimetallic nanoparticles typically lies between those of monometallic Pd (5.59 nm) and Ag (11.08 nm) nanoparticles in Pd_{100}/FA and Ag_{100}/FA, respectively.

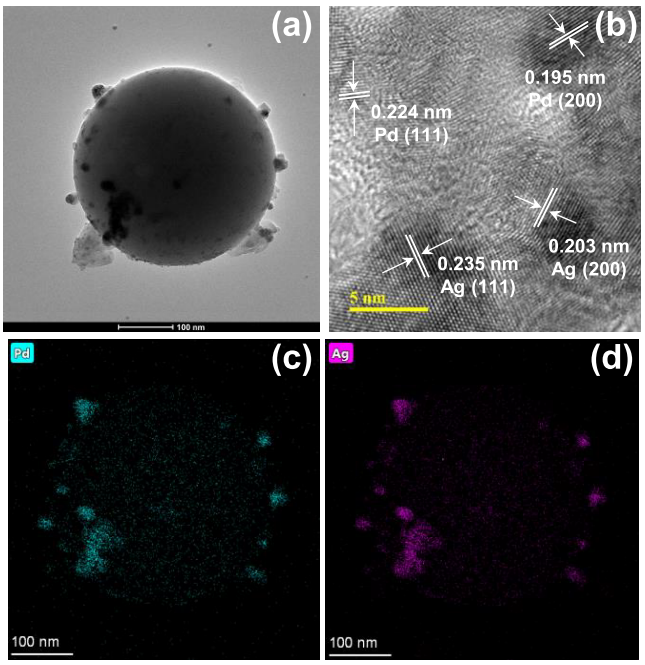

Figure 2. (a) TEM image of $Pd_{25}Ag_{75}$/FA and (b) lattice spacings for $Pd_{25}Ag_{75}$ nanoparticles. EDS element maps for Pd (c) and Ag (d).

To determine the oxidation state of the metals, XPS analysis was performed for all the FA-supported mono- and bimetallic nanoparticles (Figure 3 and Table 2). The Pd 3d binding energies appeared at 335.70 and 341.15 eV with a spin–orbit separation of 5.45 eV can be assigned to Pd $3d_{5/2}$ and Pd $3d_{3/2}$ core levels of Pd(0) nanoparticles in Pd_{100}/FA.[53] Similarly, the

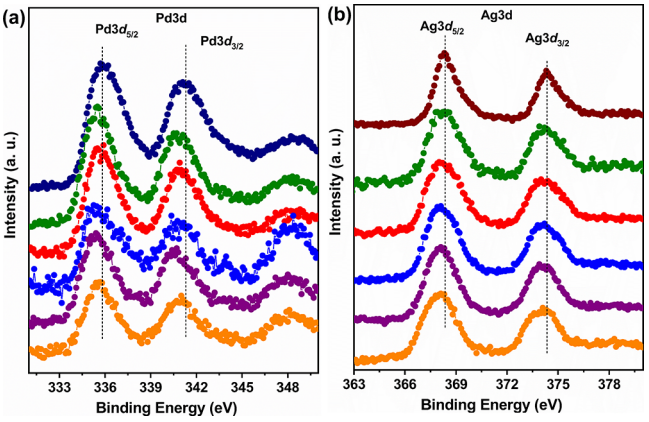

Figure 3. XPS binding energy spectra of (a) Pd 3d and (b) Ag 3d core levels for Pd_{100}/FA (navy blue), Ag_{100}/FA (wine), $Pd_{87.5}Ag_{12.5}$/FA (green), $Pd_{75}Ag_{25}$/FA (red), $Pd_{50}Ag_{50}$/FA (blue), $Pd_{25}Ag_{75}$/FA (purple), and $Pd_{12.5}Ag_{87.5}$/FA (orange).

https://doi.org/10.1021/acsomega.3c07246
ACS Omega 2024, 9, 1020–1028

Table 2. Pd and Ag Core Electron Binding Energies of the Pd_xAg_y/FA System

	binding energy (eV)			
	Pd		Ag	
Pd_xAg_y/FA	$3d_{5/2}$	$3d_{3/2}$	$3d_{5/2}$	$3d_{3/2}$
Pd_{100}/FA	335.70	341.15		
$Pd_{87.5}Ag_{12.5}$/FA	335.61	340.95	368.28	374.26
$Pd_{75}Ag_{25}$/FA	335.55	340.90	368.20	374.20
$Pd_{50}Ag_{50}$/FA	335.47	340.72	368.15	374.15
$Pd_{25}Ag_{75}$/FA	335.42	340.70	368.05	374.05
$Pd_{12.5}Ag_{87.5}$/FA	335.41	340.85	368.06	374.00
Ag_{100}/FA			368.35	374.35

binding energies appeared at 368.35 and 374.35 eV with a spin−orbit separation of 6.0 eV can be assigned to Ag $3d_{5/2}$ and Ag $3d_{3/2}$ cores for Ag(0) nanoparticles in Ag_{100}/FA.[54] A difference in spin−orbit separation of approximately 5.4 and 6.0 eV for all the bimetallic systems suggests the formation of zerovalent Pd and Ag nanoparticles, respectively, in freshly prepared Pd_xAg_y/FA samples. Notably, for the bimetallic systems, binding energies for both Pd and Ag 3d core levels shifted to a lower value than those for analogous monometallic systems. A similar observation was recently reported for the TiO_2-supported Pd_xAg_y bimetallic system.[55] Such shifting of binding energy is indicative of charge transfer between contacting Pd and Ag atoms due to the formation of alloy structure.[19,29,56,57] For the bimetallic Pd−Ag alloy system, Pd and Ag atoms are reported to lose s and p (non-d electrons) but gain d electrons.[58] Such changes in charge distribution in the bimetallic alloy system were reported to be beneficial to achieve better catalytic activity compared with monometallic analogues.[59,60]

Overall, the PXRD, TEM, and EDS elemental mapping data suggest the coexistence of Pd and Ag forming alloy structures in all the Pd_xAg_y/FA bimetallic nanostructures. In addition, shifting of binding energies for the Pd_{3d} and Ag_{3d} core electrons of the Pd and Ag atoms in Pd_xAg_y/FA supports the charge redistribution between Pd and Ag centers.

The catalytic activity of FA-supported nanomaterials was evaluated toward the reduction of 4-NP to 4-AP using aqueous $NaBH_4$ at room temperature (Scheme 1). Although the reduction of 4-NP by $NaBH_4$ is proposed to be thermodynamically favorable ($\Delta E^0 = (E^0(4NP/4AP) - E^0(H_3BO_3/BH_4^-) = -0.76 - (-1.33) = 0.67$ V), this reaction was found to be kinetically restricted in the absence of an efficient catalyst.[61] Initially, the addition of $NaBH_4$ into a solution of 4-NP (λ_{max} = 317 nm) resulted in the shifting of λ_{max} to a stronger band at 400 nm due to the formation of 4-nitrophenolate ion (Figure S24),[62] which can be catalytically reduced to 4-aminopenolate ion by the addition of dispersed Pd_xAg_y/FA nanoparticles in water. The latter reduction process could be monitored by a decrease in the intensity of the absorption band at 400 nm and simultaneous appearance of a new band around 300 nm due to the formation of amino phenolate ion (Figure 4a−e).

The catalytic rate constants of $Pd_{87.5}Ag_{12.5}$/FA ($k_{Pd87.5Ag12.5}$ = 0.430 min^{-1}), $Pd_{75}Ag_{25}$/FA ($k_{Pd75Ag25}$ = 0.650 min^{-1}), $Pd_{50}Ag_{50}$/FA ($k_{Pd50Ag50}$ = 0.717 min^{-1}), $Pd_{25}Ag_{75}$/FA ($k_{Pd25Ag75}$ = 1.050 min^{-1}), and $Pd_{12.5}Ag_{87.5}$/FA ($k_{Pd12.5Ag87.5}$ = 0.826 min^{-1}) systems were determined by plotting $-\ln(C/C_0)$ vs time (Figure 4f). A linear relation between $\ln(C/C_0)$ and time suggests that the reduction of 4-NP using $NaBH_4$ follows pseudo-first-order reaction kinetics. Rate constants for

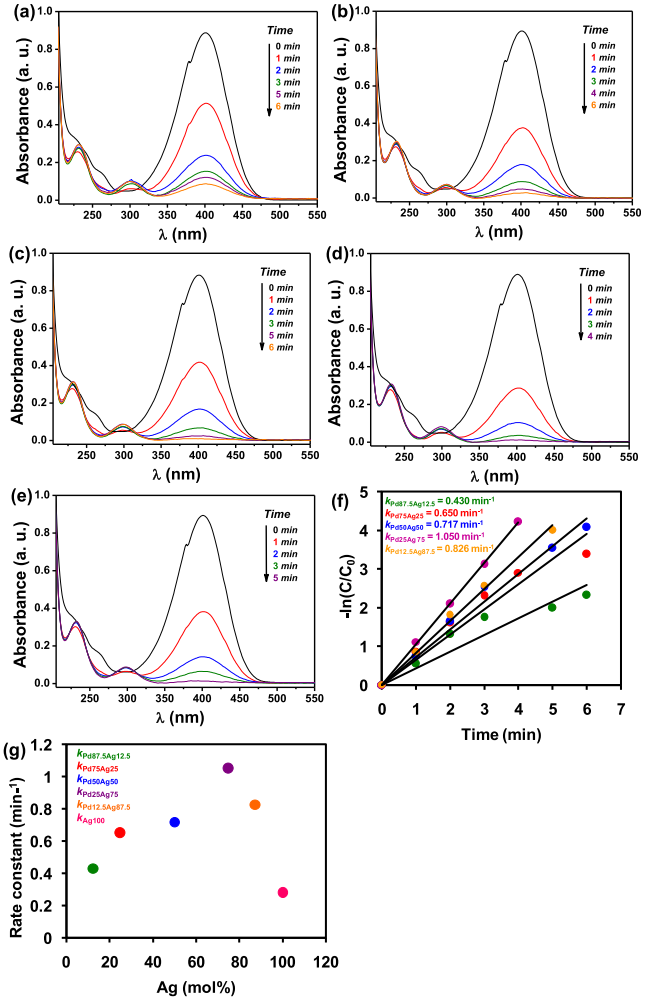

Figure 4. Time-monitored UV−visible spectra for the reduction of 4-nitrophenol using (a) $Pd_{87.5}Ag_{12.5}$/FA, (b) $Pd_{75}Ag_{25}$/FA, (c) $Pd_{50}Ag_{50}$/FA, (d) $Pd_{25}Ag_{75}$/FA, and (e) $Pd_{12.5}Ag_{87.5}$/FA. (f) -ln(C/C_0) vs time and (g) rate constant (k) vs Ag (mol %) plots.

monometallic Pd_{100}/FA (k_{Pd100} = 0.246 min^{-1}), Ag_{100}/FA (k_{Ag100} = 0.277 min^{-1}), and their physical mixture (Pd_{100}/FA + Ag_{100}/FA) ($k_{Pd100+Ag100}$ = 0.340 min^{-1}) could also be estimated under identical reaction conditions (Figures S25−S27).

By comparing rate constants among various monometallic and bimetallic nanocatalysts, it could be surmised that all the bimetallic systems are able to exhibit higher reaction rates (0.430−1.050 min^{-1}) over their monometallic analogues Pd_{100}/FA (k_{Pd100} = 0.246 min^{-1}) and Ag_{100}/FA (k_{Ag100} = 0.277 min^{-1}) as well as their physical mixture (Pd_{100}/FA + Ag_{100}/FA) ($k_{Pd100+Ag100}$ = 0.340 min^{-1}). These results therefore substantiate the synergistic effect of the bimetallic (Pd_xAg_y) nanoparticles present in the Pd_xAg_y/FA system. Interestingly, among the bimetallic nanaocatalysts, the activity was found to gradually increase with increase in Ag mol % ($Pd_{87.5}Ag_{12.5}$/FA ($k_{Pd87.5Ag12.5}$ = 0.430 min^{-1}), $Pd_{75}Ag_{25}$/FA ($k_{Pd75Ag25}$ = 0.650 min^{-1}), ($Pd_{50}Ag_{50}$/FA ($k_{Pd50Ag50}$ = 0.717 min^{-1}), and $Pd_{25}Ag_{75}$/FA ($k_{Pd25Ag75}$ = 1.050 min^{-1})); however, start to drop when the Pd:Ag ratio surpasses the threshold of 1:3 ($Pd_{12.5}Ag_{87.5}$/FA ($k_{Pd12.5Ag87.5}$= 0.826 min^{-1})). The change in the catalytic rate constants with respect to the Ag fraction (mol %) in the bimetallic systems is represented in Figure 4g.

https://doi.org/10.1021/acsomega.3c07246
ACS Omega 2024, 9, 1020−1028

Table 3. Performance of Supported Pd−Ag Bimetallic Nanocatalysts for the Reduction of 4-Nitrophenol

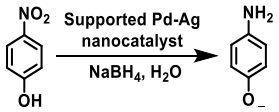

catalyst	metal used [n_{Pd+Ag} (mmol)][a]	$NaBH_4$:4-NP:metal (mol ratio)	k (min^{-1})[b]	$t_{1/2}$ (min)[c]	K (min^{-1} $mmol^{-1}$)[d]	ref
$Pd_{87.5}Ag_{12.5}$/FA	7.01×10^{-5}	214:2.14:1	0.430	1.61	6127	this work
$Pd_{75}Ag_{25}$/FA	7.01×10^{-5}	214:2.14:1	0.650	1.01	9262	this work
$Pd_{50}Ag_{50}$/FA	7.01×10^{-5}	214:2.14:1	0.717	0.97	10,217	this work
$Pd_{25}Ag_{75}$/FA	7.01×10^{-5}	214:2.14:1	1.050	0.66	14,962	this work
$Pd_{12.5}Ag_{87.5}$/FA	7.01×10^{-5}	214:2.14:1	0.826	0.84	11,770	this work
Pd_{100}/FA + Ag_{100}/FA	7.01×10^{-5}	214:2.14:1	0.340	2.02	6843	this work
Pd−Ag/dendrites	9.27×10^{-3}	3:0.02:1	2.34	0.29	252	19
Ag@Pd/Fe_3O_4	3.17×10^{-4}	125:0.9:1	1.98	0.35	6234	26
Ag@Pd/graphene	9.89×10^{-5}	100:2:1	0.5202	1.33	5257	51
Pd@Ag/SP[e]	6.27×10^{-4}	1944:0.28:1	2.0058	0.34	3197	63
Pd−Ag/rGO[f]	3.57×10^{-4}	1399:0.98:1	2.19	0.32	6126	64
Pd−Ag/PDA-rGO[g]	2.14×10^{-5}	9000:18:1	0.324	2.14	15,161	65
Pd−Ag/rGO[f]	2.45×10^{-2}	10:0.24:1	0.2413	2.87	10	66
Pd−Ag/biopolymer	NA[h]	1000:1	0.395	1.75		67

[a] n_{Pd+Ag} = mmol of Ag + Pd used for catalysis. [b] Determined from the slope of $\ln(C/C_0)$ vs t plots. [c] $t_{1/2}$ = half-life reaction time ($t_{1/2} = 0.693/k$). [d] Normalized rate constant $K = [k\ (min^{-1})/n_{Pd+Ag}\ (mmol)]$.[68] [e] SP = *Spirulina platensis*. [f] rGO = reduced graphene oxide. [g] PDA-rGO = polydopamine-reduced graphene oxide. [h] NA = not available.

Overall, catalytic results demonstrate the fact that the formation of an alloy structure, evident by PXRD analysis and EDS elemental mapping, in the FA-supported bimetallic nanocatalysts played a crucial role in achieving superior catalytic performance. As supported by XPS analysis, the redistribution of electron charge density at the Pd−Ag interface is presumed to act as an electron donor to the substrate.[60] Additionally, the presence of small Pd_xAg_y nanocrystallites (indicated by PXRD and TEM analysis) in bimetallic systems also appears to be more beneficial.

To comprehend the catalytic nitrophenol reduction efficiency of Pd_xAg_y/FA systems over other literature known supported Pd−Ag bimetallic nanocatalysts, the rate constant (k), half-life reaction time ($t_{1/2}$), and normalized rate constant (K) data are compared in Table 3, which shows that all the FA-supported Pd_xAg_y nanocatalysts can achieve comparable rate constants (k = 0.43−1.05 min^{-1}) and half-life reaction time ($t_{1/2}$= 1.61−0.66 min). However, an outstanding normalized rate constant (K = 14,962 min^{-1} $mmol^{-1}$, calculated on the basis of rate constant per mol of metal atoms) could be achieved by $Pd_{25}Ag_{75}$/FA system. Therefore, tuning of the Pd:Ag ratio turned out to be an important aspect to attain an optimum synergistic effect of the bimetallic nanocatalysts.

Next, we studied the reusability of the best-performing catalyst system $Pd_{25}Ag_{75}$/FA. As evident from conversion efficiency plots (Figure 5), no significant change in conversion was observed up to five catalytic cycles examined. The noticeable minor loss of the activity could be due to unavoidable dissolution and Ostwald ripening of the metal nanoparticles during the catalytic procedures.[69] Moreover, from TEM and HR-TEM images (Figure S28) of the used $Pd_{25}Ag_{75}$/FA nanocatalyst, no observable change in surface morphology could be identified. Such evidence could affirm high stability and recyclability of the system.

Depending on the nature of the catalyst and reducing agent, various types of reaction mechanisms including Langmuir−Hinshelwood, Eley−Rideal, semiconductor, and photocatalysis have been proposed in the literature for the reduction of

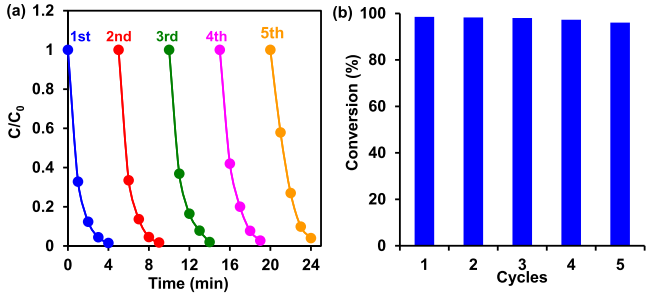

Figure 5. (a) C/C_0 vs reaction time and (b) conversion (%) plots toward the catalytic reduction of 4-NP for five successive cycles using $Pd_{25}Ag_{75}$/FA nanocatalyst.

nitroarenes into their corresponding amino derivatives.[70] The reduction of nitrophenol in particular is believed to follow the Langmuir−Hinshelwood-type mechanism when suitable metal nanoparticles are combined with $NaBH_4$ to serve as a catalyst system.[71] Considering this, a hypothetical reaction mechanism for the reduction of nitrophenol over various novel FA-supported nanonocatalysts could be proposed in Scheme S1. At the beginning, the nitrophenol is converted into nitrophenolate ion by $NaBH_4$ (Figure S24) and adsorbed over metal nanoparticles.1 Next, the hydride ion (H^-) from BH_4^- is expected to be transferred to the metal nanoparticle, followed by a secondary migration to the nitro group to initiate the reduction process.[71] After successive reduction steps, the intermediate species, such as nitroso phenolate ($^-O-C_6H_4-N=O$) and hydroxyl ($^-O-C_6H_4-NH-OH$) ions, could be generated. A further reduction of aminophenolate species is expected to lead to the formation of aminophenolate ion which gets liberated from the surface of metal nanoparticle to complete the catalytic cycle.[72,73] The processes repeat again with the adsorption of both nitrophenolate ion and BH_4^- ion on the surface of metal nanoparticle.

https://doi.org/10.1021/acsomega.3c07246
ACS Omega 2024, 9, 1020−1028

CONCLUSIONS

In summary, an amenable coprecipitation method was followed to prepare a series of FA-supported Pd_xAg_y bimetallic nanoparticles (Pd_xAg_y/FA) with varying Pd:Ag ratios. Based on PXRD analysis, the formation of alloy structure in all the bimetallic nanoparticles could be demonstrated. The EDS elemental mapping was successfully utilized to further corroborate the coexistence of both Pd and Ag atoms on the FA surface. A combination of PXRD and TEM analysis verified the dependency of crystallite size and the average size of bimetallic nanoparticles on Ag loading (mol %). The XPS analysis technique explored the charge distribution between contacting Pd−Ag sites on the FA support. Based on detailed catalytic studies it was evident that the bimetallic nanoparticles supported on FA could serve as better nanocatalysts over their monometallic analogues for the reduction of 4-nitrophenol into 4-aminophenol in the presence of aqueous $NaBH_4$. Most importantly, through tuning the Pd:Ag mole ratio, a highly active FA-supported nanocatalyst ($Pd_{25}Ag_{75}$/FA) could be prepared that exhibited a remarkably high normalized rate constant when compared to the literature reports.

ASSOCIATED CONTENT

Supporting Information

The Supporting Information is available free of charge at https://pubs.acs.org/doi/10.1021/acsomega.3c07246.

Elemental analysis data, FE-SEM and TEM images, nanoparticle size distribution plots, XPS survey spectra, and reduction of 4-nitrophenol by fly ash-supported monometallic nanoparticles (PDF)

AUTHOR INFORMATION

Corresponding Author

Niladri Maity − *Interdisciplinary Research Center for Refining and Advanced Chemicals, King Fahd University of Petroleum & Minerals, Dhahran 31261, Saudi Arabia;* orcid.org/0000-0002-0588-7849; Email: niladri.maity@kfupm.edu.sa

Authors

Aman Mishra − *Artificial Photosynthesis Laboratory, Department of Chemistry and Chemical Biology, Indian Institute of Technology (Indian School of Mines), Dhanbad 826004, India*

Samir Barman − *Interdisciplinary Research Center for Refining and Advanced Chemicals, King Fahd University of Petroleum & Minerals, Dhahran 31261, Saudi Arabia*

Sumanta Kumar Padhi − *Artificial Photosynthesis Laboratory, Department of Chemistry and Chemical Biology, Indian Institute of Technology (Indian School of Mines), Dhanbad 826004, India;* orcid.org/0000-0003-2415-0348

Binod Bihari Panda − *Department of Chemistry, Indira Gandhi Institute of Technology, Dhenkanal, Odisha 759146, India*

E. A. Jaseer − *Interdisciplinary Research Center for Refining and Advanced Chemicals, King Fahd University of Petroleum & Minerals, Dhahran 31261, Saudi Arabia;* orcid.org/0000-0002-5385-8778

Mohamed Javid − *Core Research Facilities, King Fahd University of Petroleum & Minerals, Dhahran 31261, Saudi Arabia*

Complete contact information is available at: https://pubs.acs.org/10.1021/acsomega.3c07246

Author Contributions

The manuscript was written through contributions of all authors. All authors have given approval to the final version of the manuscript.

Notes

The authors declare no competing financial interest.

ACKNOWLEDGMENTS

The authors acknowledge the support provided by Interdisciplinary Research Center for Refining and Advanced Chemicals, King Fahd University of Petroleum & Minerals (KFUPM), Dhahran 31261, Saudi Arabia for funding the project # INRC2310.

REFERENCES

(1) Ferrando, R.; Jellinek, J.; Johnston, R. L. Nanoalloys: From Theory to Applications of Alloy Clusters and Nanoparticles. *Chem. Rev.* **2008**, *108* (3), 845−910.

(2) Ghosh chaudhuri, R.; Paria, S. Core/Shell Nanoparticles: Classes, Properties, Synthesis Mechanisms, Characterization, and Applications. *Chem. Rev.* **2012**, *112* (4), 2373−2433.

(3) Loza, K.; Heggen, M.; Epple, M. Synthesis, Structure, Properties, and Applications of Bimetallic Nanoparticles of Noble Metals. *Adv. Funct. Mater.* **2020**, *30* (21), No. 1909260.

(4) Guo, S.; Dong, S.; Wang, E. Three-Dimensional Pt-on-Pd Bimetallic Nanodendrites Supported on Graphene Nanosheet: Facile Synthesis and Used as an Advanced Nanoelectrocatalyst for Methanol Oxidation. *ACS Nano* **2010**, *4* (1), 547−555.

(5) Xu, J.; Wilson, A. R.; Rathmell, A. R.; Howe, J.; Chi, M.; Wiley, B. J. Synthesis and Catalytic Properties of Au À Pd Nano Fl Owers. *ACS Nano* **2011**, *5* (8), 6119−6127.

(6) He, W.; Wu, X.; Liu, J.; Hu, X.; Zhang, K.; Hou, S.; Zhou, W.; Xie, S. Design of AgM Bimetallic Alloy Nanostructures (M = Au, Pd, Pt) with Tunable Morphology and Peroxidase-Like Activity. *Chem. Mater.* **2010**, *22*, 2988−2994.

(7) Kesavan, L.; Tiruvalam, R.; Rahim, M. H. A.; Saiman, M. I. Bin; Enache, D. I.; Jenkins, R. L.; Dimitratos, N.; Lopez-Sanchez, J. A.; Taylor, S. H.; Knight, D. W.; Kiely, C. J.; Hutchings, G. J. Solvent-Free Oxidation of Primary Carbon-Hydrogen Bonds in Toluene Using Au-Pd Alloy Nanoparticles. *Science* **2011**, *331* (6014), 195−199.

(8) Jiang, H. L.; Akita, T.; Ishida, T.; Haruta, M.; Xu, Q. Synergistic Catalysis of Au@Ag Core-Shell Nanoparticles Stabilized on Metal-Organic Framework. *J. Am. Chem. Soc.* **2011**, *133* (5), 1304−1306.

(9) Tang, S.; Vongehr, S.; Meng, X. Controllable Incorporation of Ag and Ag-Au Nanoparticles in Carbon Spheres for Tunable Optical and Catalytic Properties. *J. Mater. Chem.* **2010**, *20* (26), 5436−5445.

(10) Peng, X.; Pan, Q.; Rempel, G. L. Bimetallic Dendrimer-Encapsulated Nanoparticles as Catalysts: A Review of the Research Advances. *Chem. Soc. Rev.* **2008**, *37* (8), 1619−1628.

(11) Zhang, L.; Su, H.; Sun, M.; Wang, Y.; Wu, W.; Yu, T.; Zeng, J. Concave Cu-Pd Bimetallic Nanocrystals: Ligand-Based Co-Reduction and Mechanistic Study. *Nano Res.* **2015**, *8* (7), 2415−2430.

(12) Bondarchuk, I. S.; Mamontov, G. V. Role of PdAg Interface in Pd-Ag/SiO2 Bimetallic Catalysts in Low-Temperature Oxidation of Carbon Monoxide. *Kinet. Catal.* **2015**, *56* (3), 379−385.

(13) Lim, B.; Jiang, M.; Camargo, P. H. C.; Cho, E. C.; Tao, J.; Lu, X.; Zhu, Y.; Xia, Y. Pd-Pt Bimetallic Nanodendrites with High Activity for Oxygen Reduction. *Science* **2009**, *324* (5932), 1302−1305.

(14) Hu, S.; Che, F.; Khorasani, B.; Jeon, M.; Yoon, C. W.; Mcewen, J. S.; Scudiero, L.; Ha, S. Improving the Electrochemical Oxidation of Formic Acid by Tuning the Electronic Properties of Pd-Based Bimetallic Nanoparticles. *Appl. Catal. B Environ.* **2019**, *254*, 685−692.

(15) De corte, S.; Hennebel, T.; Fitts, J. P.; Sabbe, T.; Bliznuk, V.; Verschuere, S.; Van der lelie, D.; Verstraete, W.; Boon, N.

Biosupported Bimetallic Pd-Au Nanocatalysts for Dechlorination of Environmental Contaminants. *Environ. Sci. Technol.* **2011**, *45* (19), 8506−8513.
(16) Jiang, X.; Koizumi, N.; Guo, X.; Song, C. Bimetallic Pd-Cu Catalysts for Selective CO2 Hydrogenation to Methanol. *Appl. Catal. B Environ.* **2015**, *170*−*171*, 173−185.
(17) Ma, Q.; Sun, J.; Gao, X.; Zhang, J.; Zhao, T.; Yoneyama, Y.; Tsubaki, N. Ordered Mesoporous Alumina-Supported Bimetallic Pd-Ni Catalysts for Methane Dry Reforming Reaction. *Catal. Sci. Technol.* **2016**, *6* (17), 6542−6550.
(18) Imura, Y.; Tsujimoto, K.; Morita, C.; Kawai, T. Preparation and Catalytic Activity of Pd and Bimetallic Pd-Ni Nanowires. *Langmuir* **2014**, *30* (17), 5026−5030.
(19) Huang, J.; Vongehr, S.; Tang, S.; Lu, H.; Meng, X. Highly Catalytic Pd-Ag Bimetallic Dendrites. *J. Phys. Chem. C* **2010**, *114* (35), 15005−15010.
(20) Meng, X.; Cheng, H.; Akiyama, Y.; Hao, Y.; Qiao, W.; Yu, Y.; Zhao, F.; Fujita, S.; Arai, M. Selective Hydrogenation of Nitrobenzene to Aniline in Dense Phase Carbon Dioxide over Ni/γ-Al2O3: Significance of Molecular Interactions. *J. Catal.* **2009**, *264* (1), 1−10.
(21) Lv, J.; Wang, A.; Ma, X.; Xiang, R.; Chen, J.; Feng, J. One-Pot Synthesis of Porous Pt − Au Nanodendrites Supported on Reduced Graphene Oxide Nanosheets toward Catalytic Reduction of 4-Nitrophenol †. *J. Mater. Chem. A* **2015**, *3*, 290−296.
(22) Lv, Z.; Zhu, X.; Meng, H.; Feng, J.; Wang, A. One-Pot Synthesis of Highly Branched Pt @ Ag Core-Shell Nanoparticles as a Recyclable Catalyst with Dramatically Boosting the Catalytic Performance for 4-Nitrophenol Reduction. *J. Colloid Interface Sci.* **2019**, *538*, 349−356.
(23) Yan, Q.; Wang, X. Y.; Feng, J. J.; Mei, L. P.; Wang, A. J. Simple Fabrication of Bimetallic Platinum-Rhodium Alloyed Nano-Multipods: A Highly Effective and Recyclable Catalyst for Reduction of 4-Nitrophenol and Rhodamine B. *J. Colloid Interface Sci.* **2021**, *582*, 701−710.
(24) Oh, S. D.; Kim, M. R.; Choi, S. H.; Chun, J. H.; Lee, K. P.; Gopalan, A.; Hwang, C. G.; Sang-ho, K.; Hoon, O. J. Radiolytic Synthesis of Pd-M (M = Ag, Au, Cu, Ni and Pt) Alloy Nanoparticles and Their Use in Reduction of 4-Nitrophenol. *J. Ind. Eng. Chem.* **2008**, *14* (5), 687−692.
(25) Marimuthu, M.; Li, H.; Chen, Q. Facile Ultrasonic Synthesis of Silver-Based Bimetal Nanoparticles for Efficient Catalytic Reduction of 4-Nitrophenol. *J. Mol. Liq.* **2021**, *333*, No. 115963.
(26) Jiang, K.; Zhang, H. X.; Yang, Y. Y.; Mothes, R.; Lang, H.; Cai, W. B. Facile Synthesis of Ag@Pd Satellites-Fe3O4 Core Nanocomposites as Efficient and Reusable Hydrogenation Catalysts. *Chem. Commun.* **2011**, *47* (43), 11924−11926.
(27) Chowdhury, S. R.; Bera, K. K.; Ray, A.; Bera, P. S.; Maiyalagan, T.; Bhattacharya, S. K. Synergistic catalytic activity of palladium−silver alloy nanoparticle for anodic oxidation of ethanol in alkali. *Int. J. Hydrogen Energy* **2021**, *46*, 14212−14224.
(28) Kim, K.; Kim, K. L.; Shin, K. S. Co-Reduced Ag/Pd Bimetallic Nanoparticles: Surface Enrichment of Pd Revealed by Raman Spectroscopy. *J. Phys. Chem. C* **2011**, *115* (30), 14844−14851.
(29) Maity, N.; Sahoo, A.; Boddhula, R.; Chatterjee, S.; Patra, S.; Panda, B. B. Fly Ash Supported Pd-Ag Bimetallic Nanoparticles Exhibiting a Synergistic Catalytic Effect for the Reduction of Nitrophenol. *Dalton Trans.* **2020**, *49* (31), 11019−11026.
(30) Karakaya, I.; Thompson, W. T. The Ag-Pd (Silver-Palladium) System. *Bull. Alloy Phase Diagrams* **1988**, *9* (3), 237−243.
(31) Ranjith, K. S.; Celebioglu, A.; Uyar, T. Immobilized Pd-Ag Bimetallic Nanoparticles on Polymeric Nanofibers as an Effective Catalyst: Effective Loading of Ag with Bimetallic Functionality through Pd Nucleated Nanofibers. *Nanotechnology* **2018**, *29* (24), 245602.
(32) Sun, D.; Li, P.; Yang, B.; Xu, Y.; Huang, J.; Li, Q. Monodisperse AgPd Alloy Nanoparticles as a Highly Active Catalyst towards the Methanolysis of Ammonia Borane for Hydrogen Generation. *RSC Adv.* **2016**, *6* (107), 105940−105947.
(33) Maity, N.; Rajamohanan, P. R.; Ganapathy, S.; Gopinath, C. S.; Bhaduri, S.; Lahiri, G. K. MCM-41-Supported Organometallic-Derived Nanopalladium as a Selective Hydrogenation Catalyst. *J. Phys. Chem. C* **2008**, *112* (25), 9428−9433.
(34) Lopez-sanchez, J. A.; Dimitratos, N.; Hammond, C.; Brett, G. L.; Kesavan, L.; White, S.; Miedziak, P.; Tiruvalam, R.; Jenkins, R. L.; Carley, A. F.; Knight, D.; Kiely, C. J.; Hutchings, G. J. Facile Removal of Stabilizer-Ligands from Supported Gold Nanoparticles. *Nat. Chem.* **2011**, *3* (7), 551−556.
(35) Indra, A.; Maity, N.; Maity, P.; Bhaduri, S.; Lahiri, G. K. Control of Chemoselectivity in Hydrogenations of Substituted Nitro- and Cyano-Aromatics by Cluster-Derived Ruthenium Nanocatalysts. *J. Catal.* **2011**, *284* (2), 176−183.
(36) Maity, N.; Barman, S.; Abou-hamad, E.; D'elia, V.; Basset, J. M. Clean Chlorination of Silica Surfaces by a Single-Site Substitution Approach. *Dalt. Trans.* **2018**, *47* (12), 4301−4306.
(37) Ng, P. F.; Li, Li; Wang, S.; Zhu, Z.; Lu, G.; Yan, Z. Catalytic Ammonia Decomposition over Industrial-Waste-Supported Ru Catalysts. *Environ. Sci. Technol.* **2007**, *41* (10), 3758−3762.
(38) Shi, J. W.; Chen, S. H.; Wang, S. M.; Wu, P.; Xu, G. H. Favorable Recycling Photocatalyst TiO2/CFA: Effects of Loading Method on the Structural Property and Photocatalytic Activity. *J. Mol. Catal. A Chem.* **2009**, *303* (1−2), 141−147.
(39) Wang, S.; Zhang, F.; Cai, Q.; Zhu, L.; Luo, Z. Steam Reforming of Acetic Acid over Coal Ash Supported Fe and Ni Catalysts. *Int. J. Hydrogen Energy* **2015**, *40* (35), 11406−11413.
(40) Yusuff, A. S.; Bhonsle, A. K.; Trivedi, J.; Bangwal, D. P.; Singh, L. P.; Atray, N. Synthesis and Characterization of Coal Fly Ash Supported Zinc Oxide Catalyst for Biodiesel Production Using Used Cooking Oil as Feed. *Renew. Energy* **2021**, *170*, 302−314.
(41) Zhang, H.; Jin, M.; Wang, J.; Li, W.; Camargo, P. H. C.; Kim, M. J.; Yang, D.; Xie, Z.; Xia, Y. Synthesis of Pd-Pt Bimetallic Nanocrystals with a Concave Structure through a Bromide-Induced Galvanic Replacement Reaction. *J. Am. Chem. Soc.* **2011**, *133* (15), 6078−6089.
(42) Koenigsmann, C.; Santulli, A. C.; Gong, K.; Vukmirovic, M. B.; Zhou, W. P.; Sutter, E.; Wong, S. S.; Adzic, R. R. Enhanced Electrocatalytic Performance of Processed, Ultrathin, Supported Pd-Pt Core-Shell Nanowire Catalysts for the Oxygen Reduction Reaction. *J. Am. Chem. Soc.* **2011**, *133* (25), 9783−9795.
(43) Lim, B.; Jiang, M.; Camargo, P. H. C.; Cho, E. C.; Tao, J.; Lu, X.; Zhu, Y.; Xia, Y. Pd-Pt Bimetallic Nanodendrites with High Activity for Oxygen Reduction. *Science (80-.)* **2009**, *324* (5932), 1302−1305.
(44) Scherrer, P. Bestimmung Der Inneren Struktur Und Der Größe von Kolloidteilchen Mittels Röntgenstrahlen. In *Kolloidchemie Ein Lehrbuch*; 1912, pp 387−409.
(45) Tripathy, D.; Panda, B. B.; Maity, N. Effect of Annealing Temperature on Copper-Doped Nickel Oxide Nanomaterials for Efficient Degradation of Methylene Blue Under Solar Irradiation. *J. Electron. Mater.* **2022**, *51* (7), 3598−3605.
(46) Panda, B. B.; Tripathy, D.; Maity, N. Band Gap Tailoring and Photosensitivity Study of Al-Doped SnO2 Nanocrystallites Prepared by Sol−Gel Technique. *J. Mater. Sci. Mater. Electron.* **2022**, *33* (32), 24559−24570.
(47) Maity, N.; Wattanakit, C.; Muratsugu, S.; Ishiguro, N.; Yang, Y.; Ohkoshi, S. I.; Tada, M. Sulfoxidation on a SiO 2-Supported Ru Complex Using O 2/Aldehyde System. *Dalt. Trans.* **2012**, *41* (15), 4558−4565.
(48) Du Plessis, P. W.; Ojumu, T. V.; Petrik, L. F. Waste Minimization Protocols for the Process of Synthesizing Zeolites from South African Coal Fly Ash. *Materials* **2013**, *6* (5), 1688−1703.
(49) Patil, N. M.; Bhosale, M. A.; Bhanage, B. M. Transfer Hydrogenation of Nitroarenes into Anilines by Palladium Nanoparticles via Dehydrogenation of Dimethylamine Borane Complex. *RSC Adv.* **2015**, *5* (105), 86529−86535.
(50) Lee, K. J.; Park, S. H.; Govarthanan, M.; Hwang, P. H.; Seo, Y. S.; Cho, M.; Lee, W. H.; Lee, J. Y.; Kamala-kannan, S.; Oh, B. T. Synthesis of Silver Nanoparticles Using Cow Milk and Their

https://doi.org/10.1021/acsomega.3c07246
ACS Omega 2024, 9, 1020−1028

Antifungal Activity against Phytopathogens. *Mater. Lett.* **2013**, *105*, 128−131.
(51) Liu, C. H.; Chen, X. Q.; Hu, Y. F.; Sham, T. K.; Sun, Q. J.; Chang, J. B.; Gao, X.; Sun, X. H.; Wang, S. D. One-Pot Environmentally Friendly Approach toward Highly Catalytically Active Bimetal-Nanoparticle-Graphene Hybrids. *ACS Appl. Mater. Interfaces* **2013**, *5* (11), 5072−5079.
(52) Lu, F.; Sun, D.; Huang, J.; Du, M.; Yang, F.; Chen, H.; Hong, Y.; Li, Q. Plant-Mediated Synthesis of Ag-Pd Alloy Nanoparticles and Their Application as Catalyst toward Selective Hydrogenation. *ACS Sustain. Chem. Eng.* **2014**, *2* (5), 1212−1218.
(53) Nutt, M. O.; Heck, K. N.; Alvarez, P.; Wong, M. S. Improved Pd-on-Au Bimetallic Nanoparticle Catalysts for Aqueous-Phase Trichloroethene Hydrodechlorination. *Appl. Catal. B Environ.* **2006**, *69* (1−2), 115−125.
(54) Suh, M. P.; Moon, H. R.; Lee, E. Y.; Jang, S. Y. A Redox-Active Two-Dimensional Coordination Polymer: Preparation of Silver and Gold Nanoparticles and Crystal Dynamics on Guest Removal. *J. Am. Chem. Soc.* **2006**, *128* (14), 4710−4718.
(55) Wang, Z.; Ren, D.; He, Y.; Hong, M.; Bai, Y.; Jia, A.; Liu, X.; Tang, C.; Gong, P.; Liu, X.; Huang, W.; Zhang, Z. Tailoring Electronic Properties and Atom Utilizations of the Pd Species Supported on Anatase TiO2{101} for Efficient CO2 Hydrogenation to Formic Acid. *ACS Catal.* **2023**, *13* (15), 10056−10064.
(56) Olovsson, W.; Bech, L.; Andersen, T. H.; Li, Z.; Hoffmann, S. V.; Johansson, B.; Abrikosov, I. A.; Onsgaard, J. Core-Level Shifts for Two- and Three-Dimensional Bimetallic Pdx Cu1-x and Pdx Ag1-x Alloys on Ru(0001). *Phys. Rev. B: Condens. Matter Mater. Phys.* **2005**, *72* (7), No. 075444.
(57) Pervan, P.; Milun, M. Photoelectron Spectroscopy of the Ag/Pd (110) System. *Surf. Sci.* **1992**, *264*, 135−146.
(58) Coulthard, I.; Sham, T. K. Charge Redistribution in Pd-Ag Alloys from a Local Perspective. *Phys. Rev. Lett.* **1996**, *77* (23), 4824−4827.
(59) Kamakoti, P.; Morreale, B. D.; Ciocco, M. V.; Howard, B. H.; Killmeyer, R. P.; Cugini, A. V.; Sholl, D. S. Prediction of Hydrogen Flux Through Sulfur-Tolerant Binary Alloy Membranes. *Science (80-.)* **2005**, *307* (5709), 569−573.
(60) Sun, C. Q.; Wang, Y.; Nie, Y. G.; Mehta, B. R.; Khanuja, M.; Shivaprasad, S. M.; Sun, Y.; Pan, J. S.; Pan, L. K.; Sun, Z. Interface Quantum Trap Depression and Charge Polarization in the CuPd and AgPd Bimetallic Alloy Catalysts. *Phys. Chem. Chem. Phys.* **2010**, *12* (13), 3131−3135.
(61) Saha, S.; Pal, A.; Kundu, S.; Basu, S.; Pal, T. Photochemical Green Synthesis of Calcium-Alginate-Stabilized Ag and Au Nanoparticles and Their Catalytic Application to 4-Nitrophenol Reduction. *Langmuir* **2010**, *26* (4), 2885−2893.
(62) Baruah, B.; Gabriel, G. J.; Akbashev, M. J.; Booher, M. E. Facile Synthesis of Silver Nanoparticles Stabilized by Cationic Polynorbornenes and Their Catalytic Activity in 4-Nitrophenol Reduction. *Langmuir* **2013**, *29* (13), 4225−4234.
(63) Sun, L.; Zhang, D.; Sun, Y.; Wang, S.; Cai, J. Facile Fabrication of Highly Dispersed Pd@Ag Core−Shell Nanoparticles Embedded in Spirulina Platensis by Electroless Deposition and Their Catalytic Properties. *Adv. Funct. Mater.* **2018**, *28* (20), No. 1707231.
(64) Zhu, X. Y.; Lv, Z. S.; Feng, J. J.; Yuan, P. X.; Zhang, L.; Chen, J. R.; Wang, A. J. Controlled Fabrication of Well-Dispersed AgPd Nanoclusters Supported on Reduced Graphene Oxide with Highly Enhanced Catalytic Properties towards 4-Nitrophenol Reduction. *J. Colloid Interface Sci.* **2018**, *516*, 355−363.
(65) Alipour Ghorbani, N.; Namazi, H. Polydopamine-Graphene/Ag−Pd Nanocomposite as Sustainable Catalyst for Reduction of Nitrophenol Compounds and Dyes in Environment. *Mater. Chem. Phys.* **2019**, *234*, 38−47.
(66) Han, R.; Song, X.; Wang, Q.; Qi, Y.; Deng, G.; Zhang, A.; Wang, Q.; Chang, F.; Wu, C.; Cheng, Y. Microbial Synthesis of Graphene-Supported Highly-Dispersed Pd-Ag Bimetallic Nanoparticles and Its Catalytic Activity. *J. Chem. Technol. Biotechnol.* **2019**, *94* (10), 3375−3383.
(67) Velpula, S.; Beedu, S. R.; Rupula, K. Bimetallic Nanocomposite (Ag-Au, Ag-Pd, Au-Pd) Synthesis Using Gum Kondagogu a Natural Biopolymer and Their Catalytic Potentials in the Degradation of 4-Nitrophenol. *Int. J. Biol. Macromol.* **2021**, *190*, 159−169.
(68) Rocha, M.; Costa, P.; Sousa, C. A. D.; Pereira, C.; Rodríguez-borges, J. E.; Freire, C. L-Serine-Functionalized Montmorillonite Decorated with Au Nanoparticles: A New Highly Efficient Catalyst for the Reduction of 4-Nitrophenol. *J. Catal.* **2018**, *361*, 143−155.
(69) Bai, J.; Xiao, X.; Xue, Y. Y.; Jiang, J. X.; Zeng, J. H.; Li, X. F.; Chen, Y. Bimetallic Platinum-Rhodium Alloy Nanodendrites as Highly Active Electrocatalyst for the Ethanol Oxidation Reaction. *ACS Appl. Mater. Interfaces* **2018**, *10* (23), 19755−19763.
(70) Aditya, T.; Pal, A.; Pal, T. Nitroarene Reduction: A Trusted Model Reaction to Test Nanoparticle Catalysts. *Chem. Commun.* **2015**, *51* (46), 9410−9431.
(71) Wunder, S.; Polzer, F.; Lu, Y.; Mei, Y.; Ballauff, M. Kinetic Analysis of Catalytic Reduction of 4-Nitrophenol by Metallic Nanoparticles Immobilized in Spherical Polyelectrolyte Brushes. *J. Phys. Chem. C* **2010**, *114* (19), 8814−8820.
(72) Farhadi, S.; Kazem, M.; Siadatnasab, F. NiO Nanoparticles Prepared via Thermal Decomposition of the Bis-(Dimethylglyoximato)Nickel(II) Complex: A Novel Reusable Heterogeneous Catalyst for Fast and Efficient Microwave-Assisted Reduction of Nitroarenes with Ethanol. *Polyhedron* **2011**, *30* (4), 606−613.
(73) Gu, S.; Wunder, S.; Lu, Y.; Ballauff, M.; Fenger, R.; Rademann, K.; Jaquet, B.; Zaccone, A. Kinetic Analysis of the Catalytic Reduction of 4-Nitrophenol by Metallic Nanoparticles. *J. Phys. Chem. C* **2014**, *118* (32), 18618−18625.

https://doi.org/10.1021/acsomega.3c07246
ACS Omega 2024, 9, 1020−1028